Sensor and Simulation Notes
Note 472

IRA Variations Useful for Flexible Feed Arms

J. Scott Tyo

Electrical and Computer Engineering Department
University of New Mexico
Albuquerque, NM 87131-1356
tyo@ieee.org

Everett G. Farr, Leland H. Bowen

Farr Research, Inc.
614 Paseo Del Mar NE
Albuquerque, NM 87123

Larry L. Altgilbers
US Army/SMDC
Huntsville, AL

ABSTRACT

We examine here a number of variations of Reflector Impulse Radiating Antennas (IRAs) that are useful when the feed arms are flexible. When feed arms are built using a conducting fabric or membrane, the end of the feed arms are often contained entirely within the radius of a circular reflector, to keep the feed arms under tension. This displaces the feed arms toward the center of the reflector from the standard position where the charge center of the feed arms intersects the reflector rim. We investigate here the effect of that feed arm displacement while varying the feed impedance and feed arm position. We also investigate the effect of shaping the reflector to exclude the portion of the aperture that contributes destructively to the radiated field. For each of these configurations, we calculate the effective height, antenna gain, and sidelobe level.

1. Introduction

In this paper, we consider a number of configurations of the Impulse Radiating Antenna (IRA) that are useful with flexible feed arms. These IRA variations include the Para-IRA [1] and the Membrane IRA [2]. In such designs, the feed arms must remain under tension, so it is often easier to place the feed arms such that their outside edge intersects the outer rim of the parabolic reflector. This is different from the standard position, in which the charge center of the feed arm intersects the outer rim of the reflector. Failure to keep the feed arms within the rim of the reflector results in "floppy" feed arms, so the modification keeping the feed arms within the reflector is referred to as "non-floppy." We calculate here the effect of adjusting the position of the feed arms to the non-floppy position as it relates to gain, aperture height, and sidelobe levels.

We also calculate the effect of shaping the aperture. It known that a portion of a round aperture contributes destructively to the total radiated field on boresight [3]. This effect becomes more significant when the feed arms are adjusted to the non-floppy position. Because shaping the aperture imposes an additional cost in fabrication, we investigate here the additional benefit achieved.

Finally, we calculate the effect of varying the feed impedance from the standard value of 200 ohms. Normally, we use 200 ohms in order to make use of a 4:1 splitter balun to match to a 50-ohm feed cable. There are cases, however, where no balun can be used, due to either high voltages or a lack of space. The Para-IRA is an example of such a case. In these cases, there is no reason to confine ourselves to 200 ohms, so we calculate the effect of varying the feed impedance from the standard value of 200 ohms.

The prompt radiated fields from an IRA can be predicted from the distribution of the TEM mode in the focused aperture of the antenna. For the early time, the radiated field on boresight at position r and time t is given approximately as [4]

$$E_{rad}(r,t) = \frac{h_a}{2\pi r c f_g} \frac{dV(t')}{dt}, \tag{1}$$

where $V(t')$ is the applied voltage in retarded time and h_a is the aperture height given by

$$h_a = -\frac{f_g}{V_0} \iint_A E_y(x,y)\,dxdy. \tag{2}$$

In (2) $f_g = Z_{line}/Z_0 = Z_{line}/120\pi$ is the geometric impedance factor, V_0 is the voltage of the applied step function, and A is the area of the focused aperture. For a given feed configuration, the choice of aperture A has a significant effect on the prompt radiated field. Several authors have studied the effects of altering the aperture shape for a given feed structure in order to optimize the radiated field [3,5,6,7]. For a given feed structure and aperture outer boundary, the prompt radiated field can be maximized by removing the portions of the aperture where E_y contributes destructively to the aperture integral in (2) [3]. Furthermore, an optimum ratio between the radius of the feed

arms and the maximum radius of the circular aperture was calculated, and shown to be a function of both feed impedance and feed arm angle. For a given desired input impedance, the optimum value of ϕ_0 and aperture radius can be obtained [3]. Recent numerical [8] and experimental [9] results have demonstrated that simply changing the feed arm angle to 60° (from the horizontal) from 45° can produce an increase in aperture height of approximately 20%.

2. Feed Configurations and Aperture Heights

Unlike a typical IRA that has feed arms that intersect the circular reflector at the circle of reciprocation symmetry of the feed, flexible feed arms are usually built so their outside edge intersects the reflector at the outer radius of the feed arms, as shown in fig. 1. One notable exception is the Collapsible Impulse Radiating Antenna [9], which solves the problem of floppy feed arms with an extra support arm. This is not a viable option in either the Para-IRA or Membrane IRA. The need to use such a large radius forces the circular aperture to encompass fields that destructively contribute to the aperture height in (2). At these large radii, trimming of the focused aperture can provide a significant improvement in h_a [3]. For the purposes of this study, we considered all combinations of the following configurations:

- Feed arm angles:

1. ±45° from the horizontal
2. ±60from the horizontal

- Input Impedances

1. 150 Ω
2. 200 Ω
3. 250 Ω

- Aperture Configurations (see fig. 2)

1. Standard Aperture (S)
2. Non-Floppy Aperture (NF)
3. Non-Floppy Aperture with Exclusion Contour (NFE)

The physical size of the electrodes (b_1/b and b_2/b) for the feed arm angles and impedances listed above are given in table 1.

Z_{line}	arm angle (° from horiz)	b_1/b	b_2/b
150	60	.5810	1.7213
150	45	.7173	1.3941
200	60	.7831	1.277
200	45	.8665	1.154
250	60	.8982	1.1134
250	45	.9397	1.0642

Table 1: Size of the electrodes for the impedances and feed arm angles considered in this study.

In this study, the aperture height was computed from the TEM mode field distributions, neglecting feed blockage. The electric field of the TEM mode can be obtained as the gradient of a scalar potential that satisfies the 2-dimensional Laplace's equation on the surface of a sphere. The stereographic projection can be used to convert the spherically symmetric geometry of the TEM feed to an equivalent cylindrical structure [10]. In general, the complex potential on the 2-dimensional feed structure is obtained via a conformal transformation, and is given as

$$w(z)=u(z)+jv(z)=u(x+jy)+jv(x+jy), \tag{3}$$

where z is the complex position. When the functional form of the conformal transformation is unknown, the potential must be obtained using numerical methods. In this study, Laplace's equation was solved numerically using the method of moments. The potential in the z-plane is given as

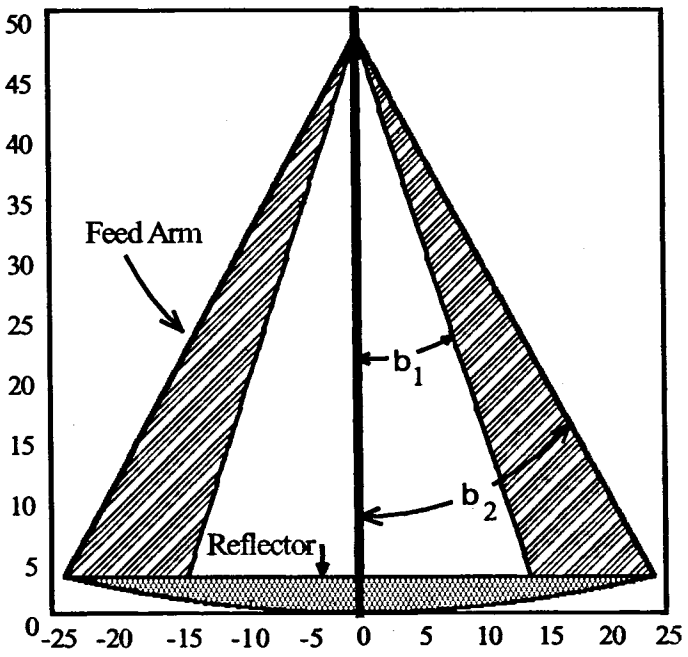

Figure 1. Angles associated with the IRA feed arms.

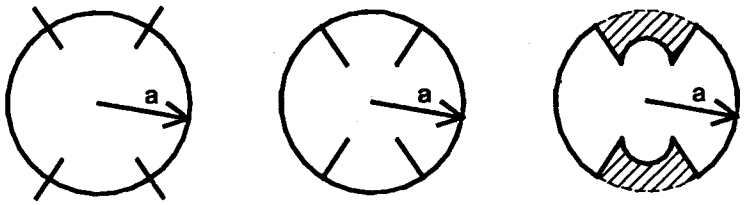

Figure 2. The three aperture configurations.

$$u(z)=\sum_i \frac{1}{4\pi\varepsilon}\oint_{C_i}\frac{\rho_s(x',y')}{|z-z'|}d\ell', \tag{4}$$

where C_i is the contour on the surface of the ith conductor and ρ_s is the (unknown) surface charge density on the conductor. Eqn. (4) is solved for ρ_s using the method of moments with the boundary conditions

$$u(z)=\pm 1 \tag{5}$$

on the electrodes. Once the charge distribution is known, the transmission line parameters can be solved, and the electric potential is given by (4). Using methods developed by Baum [5], the two-dimensional aperture integral of the electric field in (2) can be converted to a contour integral of the electric potential

$$h_a=\frac{1}{\Delta v}\oint_C u dx, \tag{6}$$

where Δv is the change in magnetic scalar potential around one of the conductors (proportional to the stored charge in the capacitor).

2.1. Computation of the Exclusion Contour

The electric potential and field line distribution for Z = 200 Ω, $\phi_0 = 60°$ and $\phi_0 = 45°$ are presented in fig. 3. As discussed previously, some of the electric field lines in the focused aperture actually contribute destructively to the surface integral in (2). To determine the areas of the aperture that should be eliminated, the contour at

$$E_y = 0 \tag{7}$$

is indicated in fig. 3. This aperture provides the maximum possible aperture height for a fixed input impedance and aperture shape [3]. The exclusion contours for the 150Ω cases are presented

in fig. 4 and the contours for the 250 Ω cases are presented in fig. 5. Once the exclusion contour is known, the aperture height for the three aperture configurations can be calculated using (6). Table 2 presents the computed values of the aperture height. To obtain the angles β_1 and β_2 in fig. 1, the standard formulas in [10] can be applied.

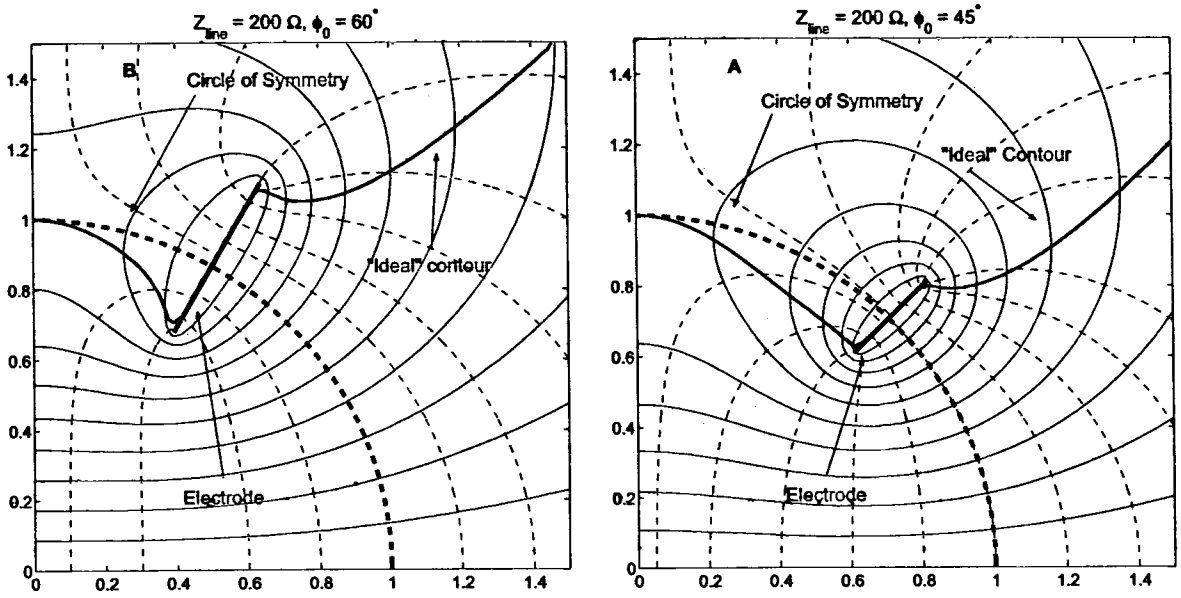

Figure 3: Potential and field distributions for the two 200 Ω cases considered here. Field lines are dashed, equipotentials are solid. The ideal contour is indicated in bold. Note that there are regions above the ideal contour where electric field contributes destructively to the integral in (2).

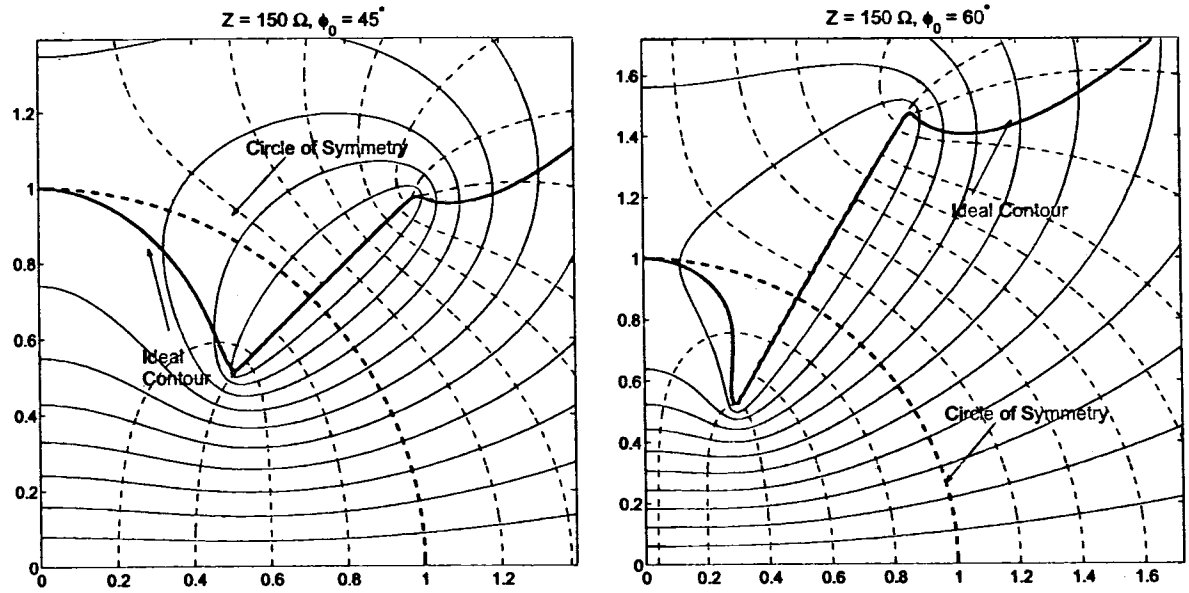

Figure 4: Exclusion contours for 150 Ω feeds.

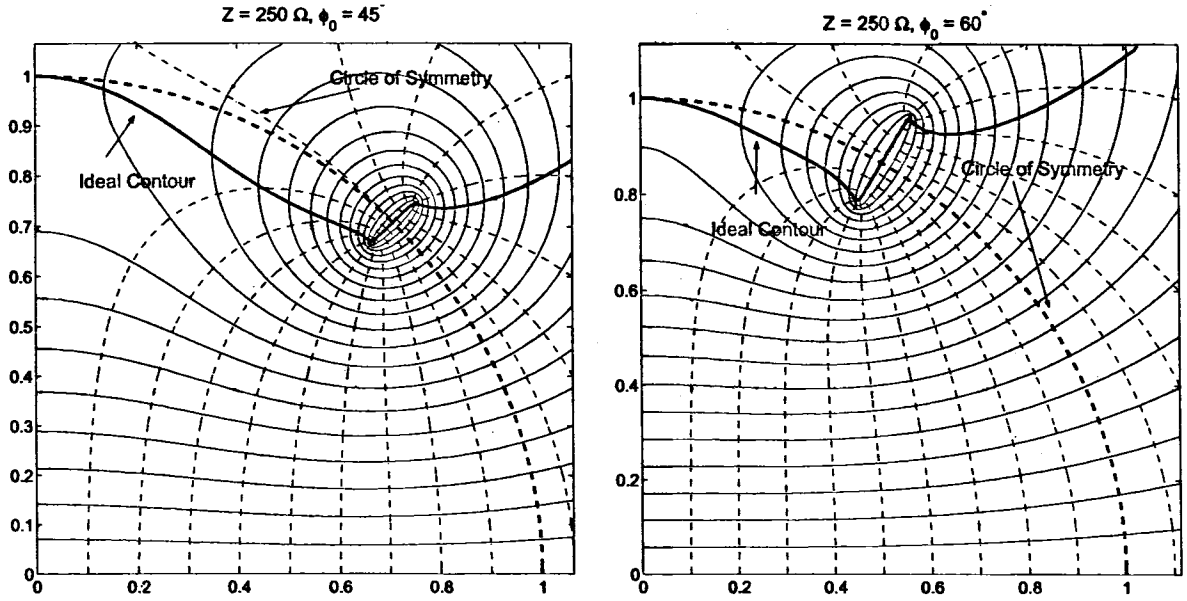

Figure 5: Exclusion contours for 250 Ω feeds.

Z_{line}	arm angle (° from horiz)	config	h_a/a
150	60	S	.6198
150	60	NF	.5413
150	60	NFE	.5996
150	45	S	.5761
150	45	NF	.5212
150	45	NFE	.6075
200	60	S	.7431
200	60	NF	.6884
200	60	NFE	.7401
200	45	S	.6463
200	45	NF	.6159
200	45	NFE	.6823
250	60	S	.8093
250	60	NF	.7800
250	60	NFE	.8140
250	45	S	.6799
250	45	NF	.6652
250	45	NFE	.7071

Table 2: Aperture height and physical parameters for the IRA configurations tested here. To get from b_1 and b_2 to the feed arm angles β_1 and β_2, follow the standard methods presented in [10]. Note that the highest aperture heights occur for the 250 Ω impedances, but the aperture efficiencies are slightly lower than the 200 Ω cases because of the factor of f_g that appears in the denominator of (1).

3. Effective Gain and Off-Boresight Performance

The results presented in section 2 are for radiated field in the direction of focus of the antenna optic. In order to assess the off boresight fields, we must return to the theory of aperture antennas. The coordinate system for the below discussion is presented in fig. 6. The theory here parallels the development presented in SSN 306 [11] (in the direction of focus) and SSN 358 [12] (off-boresight). Using conventional aperture antenna theory [13], we assume that the aperture plane exists at $z = 0$ with electric and magnetic fields in the aperture defined by the TEM mode and fields outside the aperture equal to zero. We further assume that the region of space for $z < 0$ is occupied by perfect electrical conductor. We can replace the tangential fields in the aperture by equivalent electric and magnetic surface currents. The PEC half-space shorts out the equivalent electric currents[1], so we only need to consider the magnetic surface currents defined by

$$\mathbf{M}(x',y',t) = -2\hat{\mathbf{z}} \times \mathbf{E}_{TEM}(x',y',t), \tag{8}$$

where $\mathbf{E}_{TEM}$ is the electric field of the TEM mode. The primed coordinates indicate the aperture (source) point. Using the time domain Greens function, the vector electric potential at position $\mathbf{r}$ and time t is

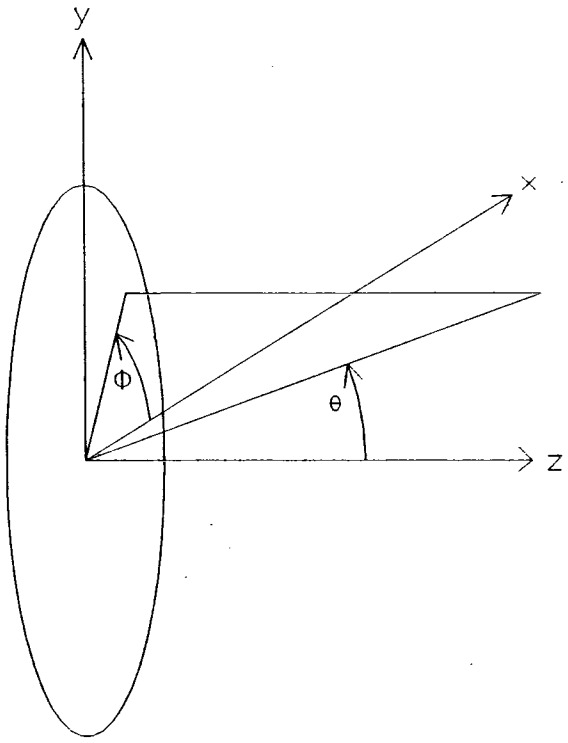

Figure 6: Coordinates used for the off-boresight radiation calculations.

[1] This assumption means that we can only compute the fields *far* from the aperture plane

$$\mathbf{F}(\mathbf{r},t)=\frac{\varepsilon}{4\pi}\iint_A \frac{\mathbf{M}\left(\mathbf{r}',t-\frac{R}{c}\right)}{R}dx'dy', \tag{9}$$

where $R=|\mathbf{r}-\mathbf{r}'|$. Using the law of cosines and the first two terms of the Taylor series for we can approximate

$$R\approx r-\sin\theta\cos\phi x'-\sin\theta\sin\phi y', \tag{10}$$

and (9) becomes

$$\begin{aligned}\mathbf{F}(\mathbf{r},t)=\frac{\varepsilon}{2\pi r}\iint_A\Bigg(&-\hat{\mathbf{y}}E_x\left(x',y',t-\frac{r}{c}+\frac{\sin\theta\cos\phi x'+\sin\theta\sin\phi y'}{c}\right)+\\ &\hat{\mathbf{x}}E_y\left(x',y',t-\frac{r}{c}+\frac{\sin\theta\cos\phi x'+\sin\theta\sin\phi y'}{c}\right)\Bigg)dx'dy'.\end{aligned} \tag{11}$$

We will now evaluate the electric field in the E- and H-planes for the co-polarized component (principal polarization)[2]. This polarization is due to the y-component of the TEM mode E-field, which produces a Magnetic current (and F-field) that is in the x-direction. The electric field is obtained from the vector potential as

$$\mathbf{E}(\mathbf{r},t)=-\frac{1}{\varepsilon}\nabla\times(F_x\hat{\mathbf{x}}) \tag{12}$$

Eqn. (12) can be evaluated in spherical coordinates using

$$\mathbf{E}=\nabla F_x\times\hat{\mathbf{x}}=\left(\frac{\partial F_x}{\partial r}\hat{\mathbf{r}}+\frac{1}{r}\frac{\partial F_x}{\partial\theta}\hat{\theta}-\frac{1}{r\sin\theta}\frac{\partial F_x}{\partial\phi}\hat{\phi}\right)\times\hat{\mathbf{x}}. \tag{13}$$

The gradient of F_x is approximately

$$\nabla F_x\approx-\hat{\mathbf{r}}\frac{\varepsilon}{2\pi rc}\frac{d}{dt}\left(\iint_A E_y\left(x',y',t-\frac{r}{c}+\frac{\sin\theta\cos\phi x'+\sin\theta\sin\phi y'}{c}\right)\right). \tag{14}$$

Terms of order r^{-2} or higher have been ignored in obtaining the approximation in (14). Taking the cross product in (13) produces

[2] We will be ignoring the cross-pol calculations in this analysis. While the aperture fields are important for computing crosspol at higher frequencies, experimental evidence indicates that factors surrounding the physical construction of the antenna have a greater influence on the cross polarization [9].

$$\mathbf{E}(\mathbf{r},t)=\frac{1}{2\pi rc}\frac{d}{dt}\left(\iint_A E_y(x',y',t')dx'dy'\right)\cdot\left[\hat{\phi}\cos\theta\cos\phi+\hat{\theta}\sin\phi\right]. \tag{15}$$

The variable t' in (15) is retarded time. In the H-plane we have $\phi=0$, and we compute the radiation as a function of the polar angle θ (see fig. 6). The $\hat{\theta}$ term in (15) disappears, and the radiated E-field is in the $\hat{\phi}$ direction. We must evaluate the following assuming step excitation

$$E_{\phi}^{(h)}(\theta,t)=\frac{\cos\theta}{2\pi rc}\frac{d}{dt}\left(\iint_A E_y(x',y')u(t')dx'dy'\right) \tag{16}$$

$$E_{\phi}^{(h)}(\theta,t)=\frac{\cos\theta}{2\pi rc}\iint_A E_y(x',y')\delta\left(t''+\frac{\sin\theta x'}{c}\right)dx'dy' \tag{17}$$

$$E_{\phi}^{(h)}(\theta,t)=\frac{\cot\theta}{2\pi r}\int E_y\left(-\frac{ct''}{\sin\theta},y'\right)dy'=\frac{V_0\cot\theta}{2\pi r}\Phi^{(h)}\left(-\frac{ct''}{\sin\theta}\right) \tag{18}$$

In the above equations, $t''=t-r/c$ is the retarded time at the center of the aperture. A similar analysis in the E-plane yields

$$E_{\theta}^{(e)}(\theta,t)=\frac{1}{2\pi r\sin\theta}\int E_y\left(x',-\frac{ct''}{\sin\theta}\right)dx'=\frac{V_0}{2\pi r\sin\theta}\Phi^{(e)}\left(-\frac{ct''}{\sin\theta}\right). \tag{19}$$

To find the sidelobes as a function of θ for a given frequency ω, we take the Fourier transforms of (18) and (19) to get

$$E_{\phi}^{(h)}(\theta,\omega)=\frac{V_0\cos\theta}{2\pi rc}\tilde{\Phi}^{(h)}\left(-\frac{\omega\sin\theta}{c}\right) \text{ and} \tag{20}$$

$$E_{\theta}^{(e)}(\theta,\omega)=\frac{V_0}{2\pi rc}\tilde{\Phi}^{(e)}\left(-\frac{\omega\sin\theta}{c}\right). \tag{21}$$

To obtain the effective gain, we divide the local power density defined by (20) and (21) by the total power available to the antenna[3]. The average power density is given as

$$S_{av}(\omega)=\frac{P_{tot}(\omega)}{4\pi r^2}=\frac{1}{8\pi r^2\omega^2 Z_{line}}, \tag{22}$$

where step excitation is assumed to find P_{tot}. The effective gain in the H- and E-planes are

[3] The effective gain takes into account both the directivity of the antenna and the fraction of the power that is reflected at the antenna feed.

$$G^{(h)}(\theta,\omega) = 4\pi f_g \cos^2\theta \frac{f^2 \left|\tilde{\Phi}^{(h)}\left(-\frac{\omega \sin\theta}{c}\right)\right|^2}{c^2} \text{ and} \tag{23}$$

$$G^{(e)}(\theta,\omega) = 4\pi f_g \frac{f^2 \left|\tilde{\Phi}^{(e)}\left(-\frac{\omega \sin\theta}{c}\right)\right|^2}{c^2}. \tag{24}$$

3.1. Interpretation

If we examine the Fourier transforms of $\Phi^{(e)}$ and $\Phi^{(h)}$ for the various configurations, we can determine the sidelobe performance in each case. We will examine the 200 Ω case first (and most closely).

Eqn. (23) tells us that the antenna pattern *shape* is independent of frequency. This is because the aperture illumination is identical for all frequencies (since the feed is TEM). The only thing that changes as a function of frequency is the *location* in angular space of the sidelobes. Fig. 7 and fig. 8 show the important information for feed arms at 45° and 60° from the horizontal, respectively. In each of the four plots presented in these figures, there are three curves. The dashed red curve is the standard aperture that focuses the circle of symmetry with no aperture trimming. The green curve (dash-dot) presents the non-floppy aperture. The solid blue curve is the NFE case.

In each set of four figures, the upper left plot is $\Phi^{(h)}$, the upper right plot is $\Phi^{(e)}$, the lower left plot is the magnitude of the Fourier transform of $\Phi^{(h)}$ squared , and the lower right plot is the magnitude of the Fourier transform of $\Phi^{(e)}$ squared. The x-axis of the sidelobe plots is labeled as $\omega \sin\theta/c$. As the frequency increases, a smaller angle θ results in the same spot on the x-axis of these plots. For example, for a 1-m radius aperture at $f = 1$ GHz, $\omega/c = 20.9$, and $\omega \sin\theta/c = 1$ corresponds to an angle of 2.73°. The y-axes of these plots present gain normalized to the size of the aperture (in wavelengths) . The factor of $\cos^2\theta$ has minimal effect on the gain, and results in a decrease in gain of less than 0.5 dB for angles less than 20° (less than 0.15 dB for angles less than 10°). Even though the pattern has the same shape as a function of frequency, the absolute gain increases. This is because the aperture size is fixed in length units, but increases in size in wavelength units for the higher frequencies. At $f = 1$ GHz, we add 18.7 dB to get the absolute effective gain. Table 3 presents the peak gain and the maximum sidelobes in the E- and H-planes for the 4-arm IRAs studied thus far.

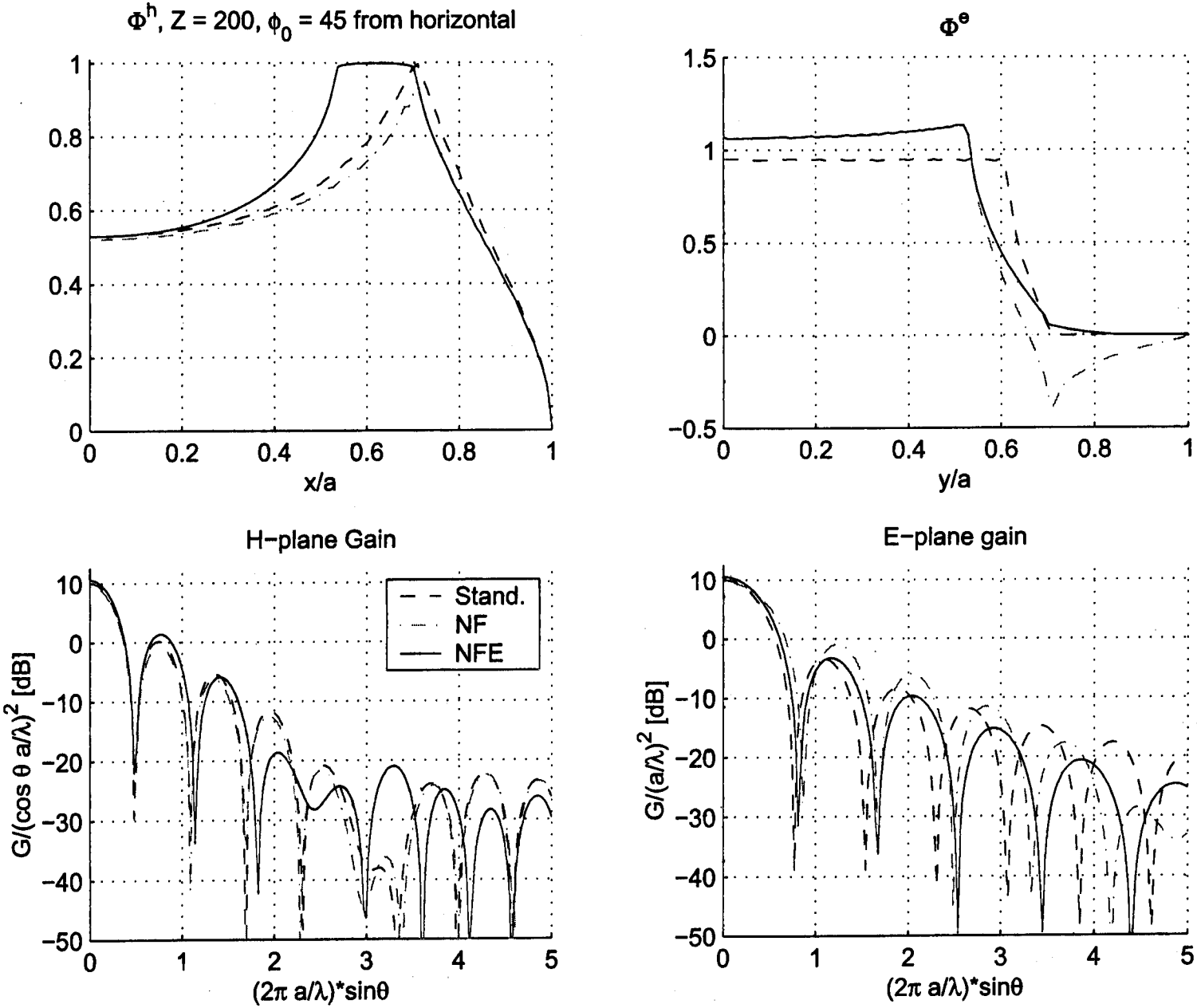

Figure 7: Off-boresight radiation in the time and frequency domains, in the E- and H-planes for the 200 Ω, 45° configurations.

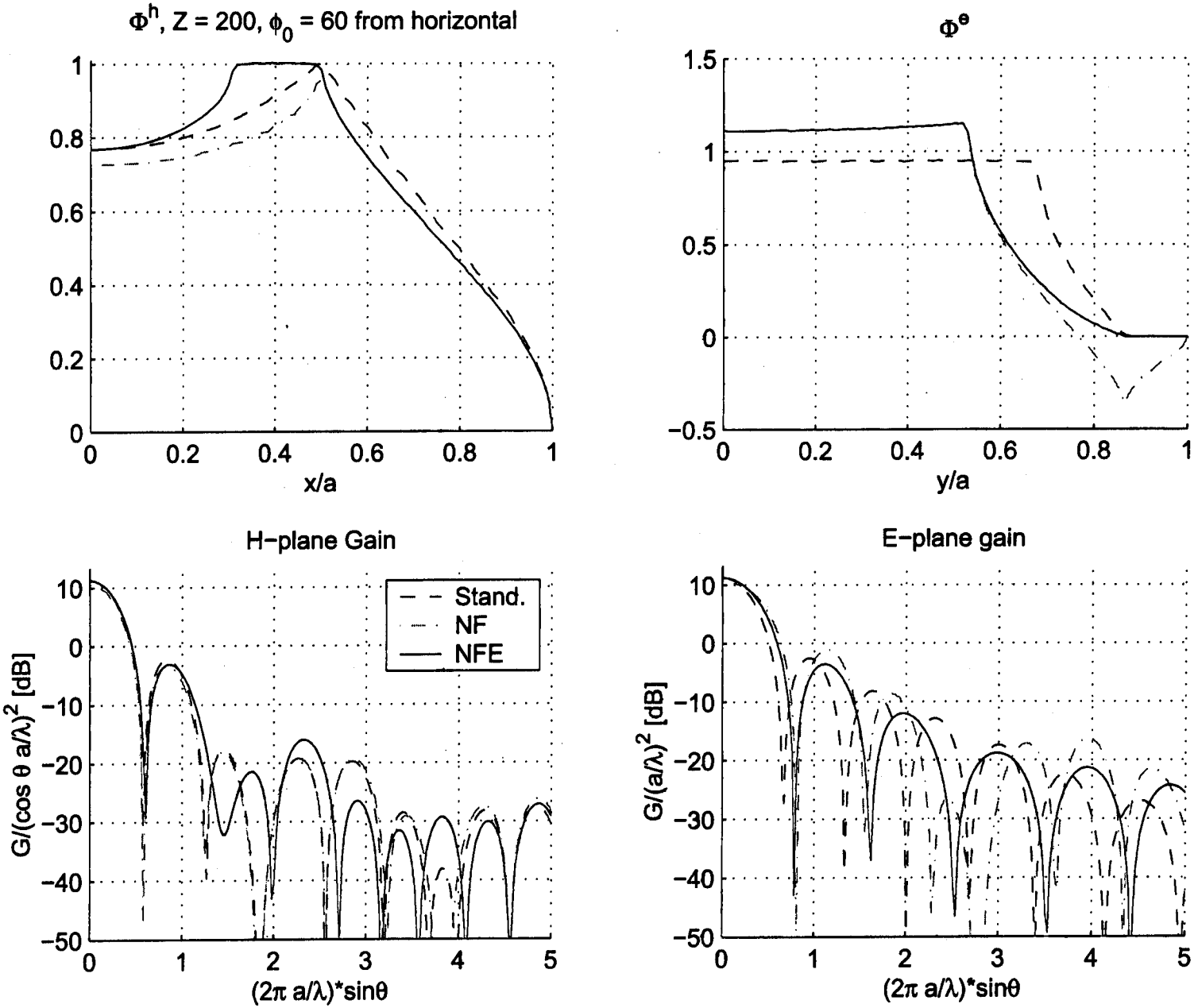

Figure 8: Off-boresight radiation in the time and frequency domains, in the E- and H-planes for the 200 Ω, 60° configurations.

Z_{line} Ω	arm angle (° from horiz)	Config	Peak Gain/$(a/\lambda)^2$ (dB)	H-Plane		E-Plane	
				SLL (dB down)	beamwidth $\omega \sin\theta / c$	SLL (dB down)	beamwidth $\omega \sin\theta / c$
150	45	S	10.9	11.1	.194	14.3	.314
150	45	NF	8.85	11.5	.208	12.4	.500
150	45	NFE	12.1	10.8	.208	17.4	.375
150	60	S	12.7	15.0	.218	12.3	.289
150	60	NF	9.58	14.6	.229	12.0	.375
150	60	NFE	11.8	16.7	.229	15.2	.312
200	45	S	10.2	9.90	.199	13.5	.289
200	45	NF	9.21	10.3	.187	10.6	.375
200	45	NFE	11.5	9.2	.187	13.8	.312
200	60	S	13.5	13.7	.212	13.8	.245
200	60	NF	11.5	14.0	.229	11.7	.333
200	60	NFE	13.5	14.3	.229	14.9	.292
250	45	S	8.96	9.24	.196	13.3	.274
250	45	NF	8.56	9.53	.187	11.7	.312
250	45	NFE	9.95	8.62	.187	13.4	.271
250	60	S	12.7	12.5	.225	13.4	.225
250	60	NF	11.8	13.0	.229	12.0	.271
250	60	NFE	13.0	12.6	.229	13.3	.250

Table 3: Sidelobe performance. Gain is normalized to the size of the aperture in wavelengths. The largest sidelobe in the *E*- and *H*-planes are identified by both gain and position in angular space.

Fig. 9 and fig. 10 show the overall sidelobe information for the 150 Ω case. In order to have lower impedances at the same feed arm angle, the electrode width must increase. This wider electrode affects the "flat" portion of the $\Phi^{(e)}$ curve, resulting in a much wider beam in the E-plane than at higher impedances. This wider beam has the general effect of also lowering the sidelobes, as can be seen in table 3. The results for the 250 Ω case are presented in figs. 11 and 12.

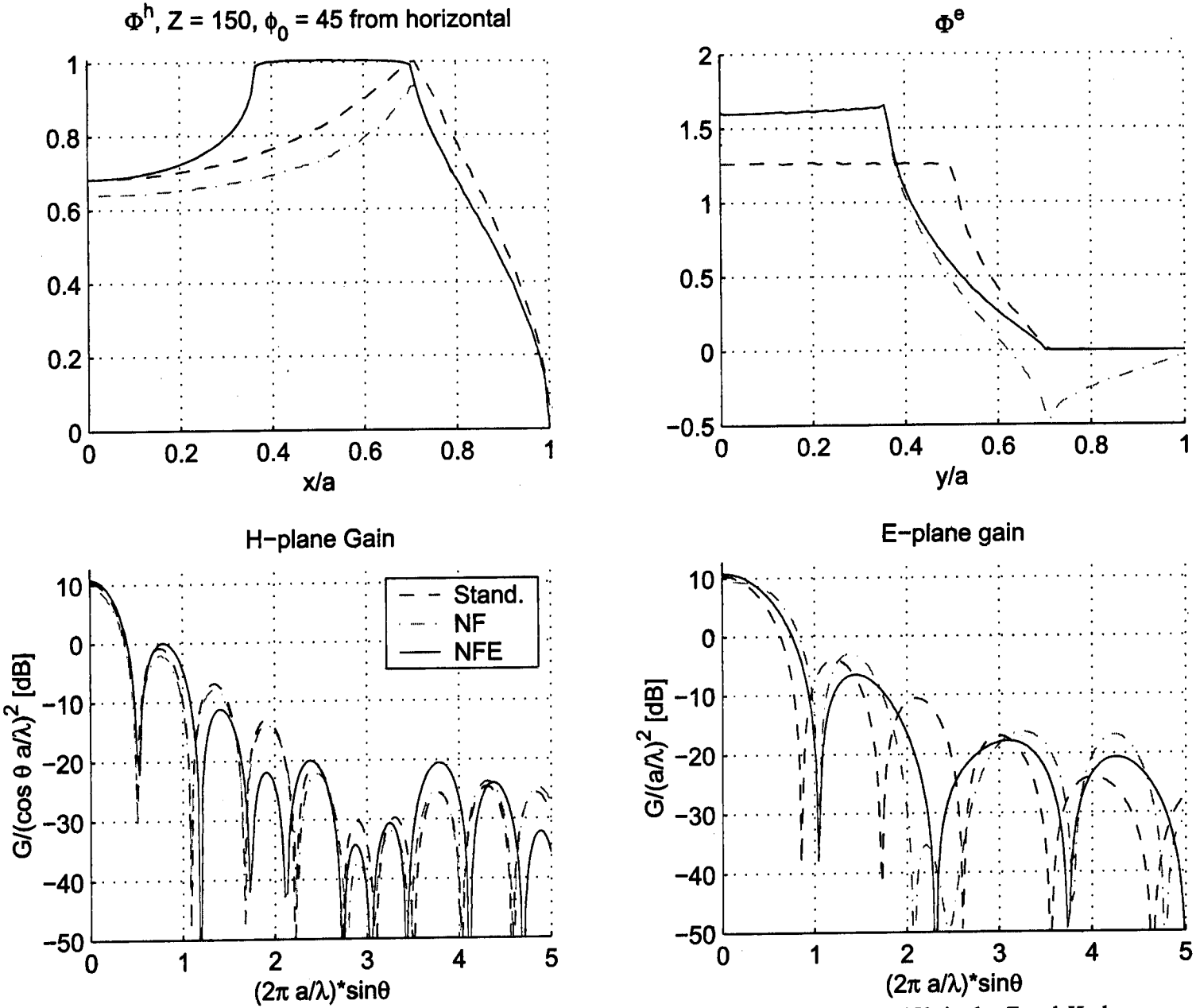

Figure 9: Off boresight radiation in the time- and frequency-domains for Z = 150 Ω, ϕ_0=45°, in the *E* and *H*-plane.

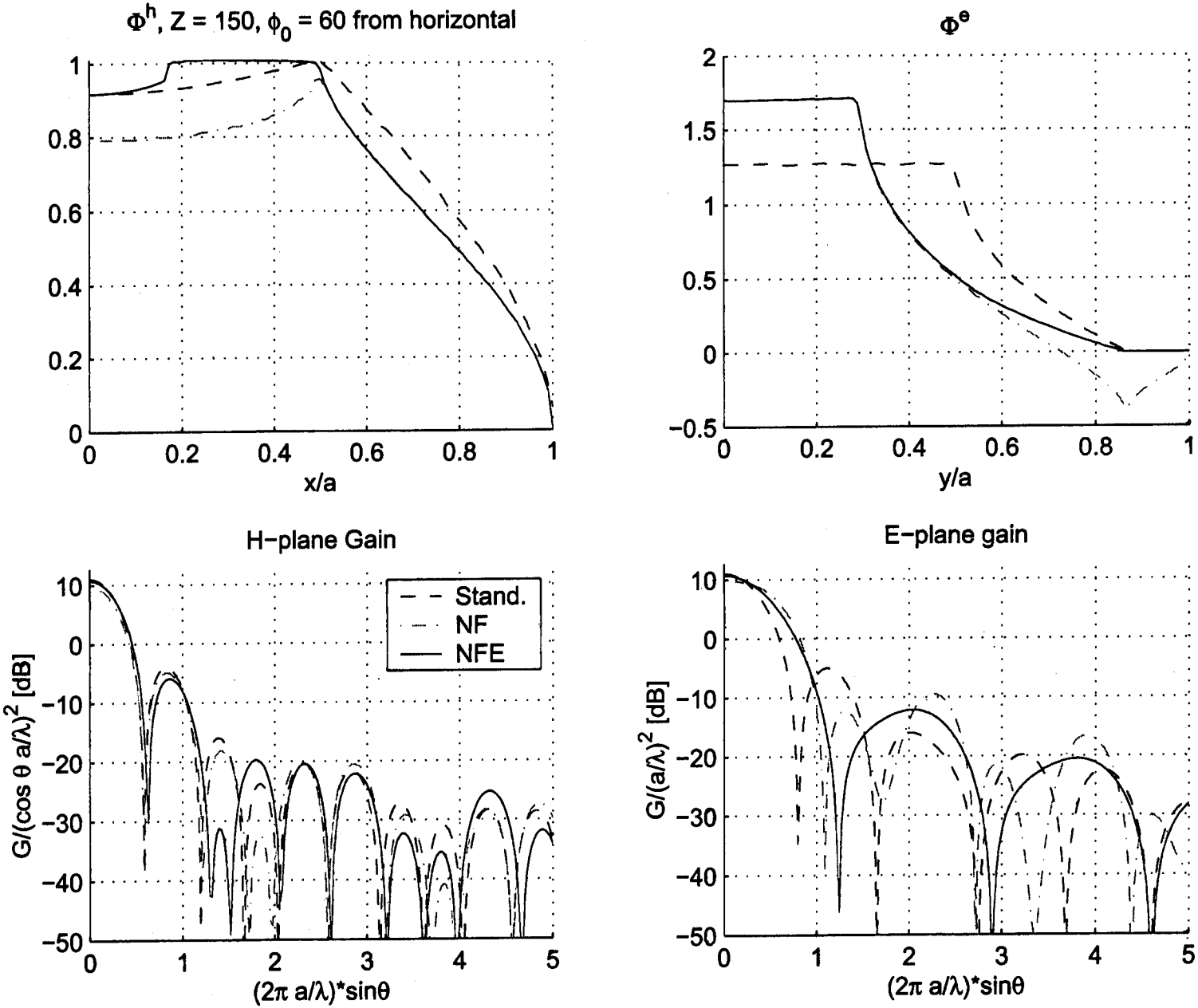

Figure 10: Off boresight radiation in the time-and frequency domains for Z = 150 Ω, ϕ_0=60°, in the *E* and *H*-planes.

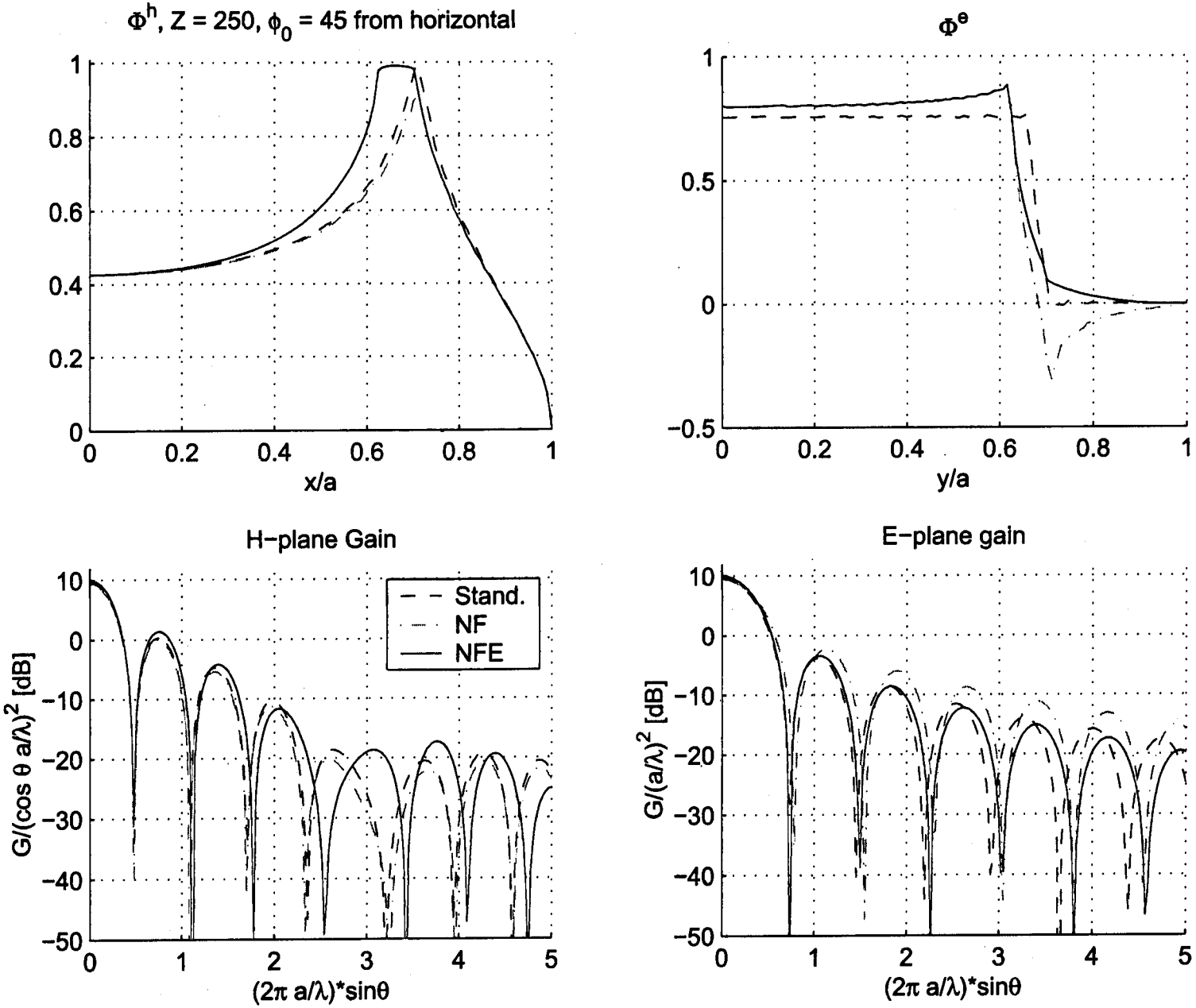

Figure 11: Off boresight radiation in the time- and frequency-domains for Z = 250 Ω, ϕ_0 = 45° in the *E* and *H*-planes.

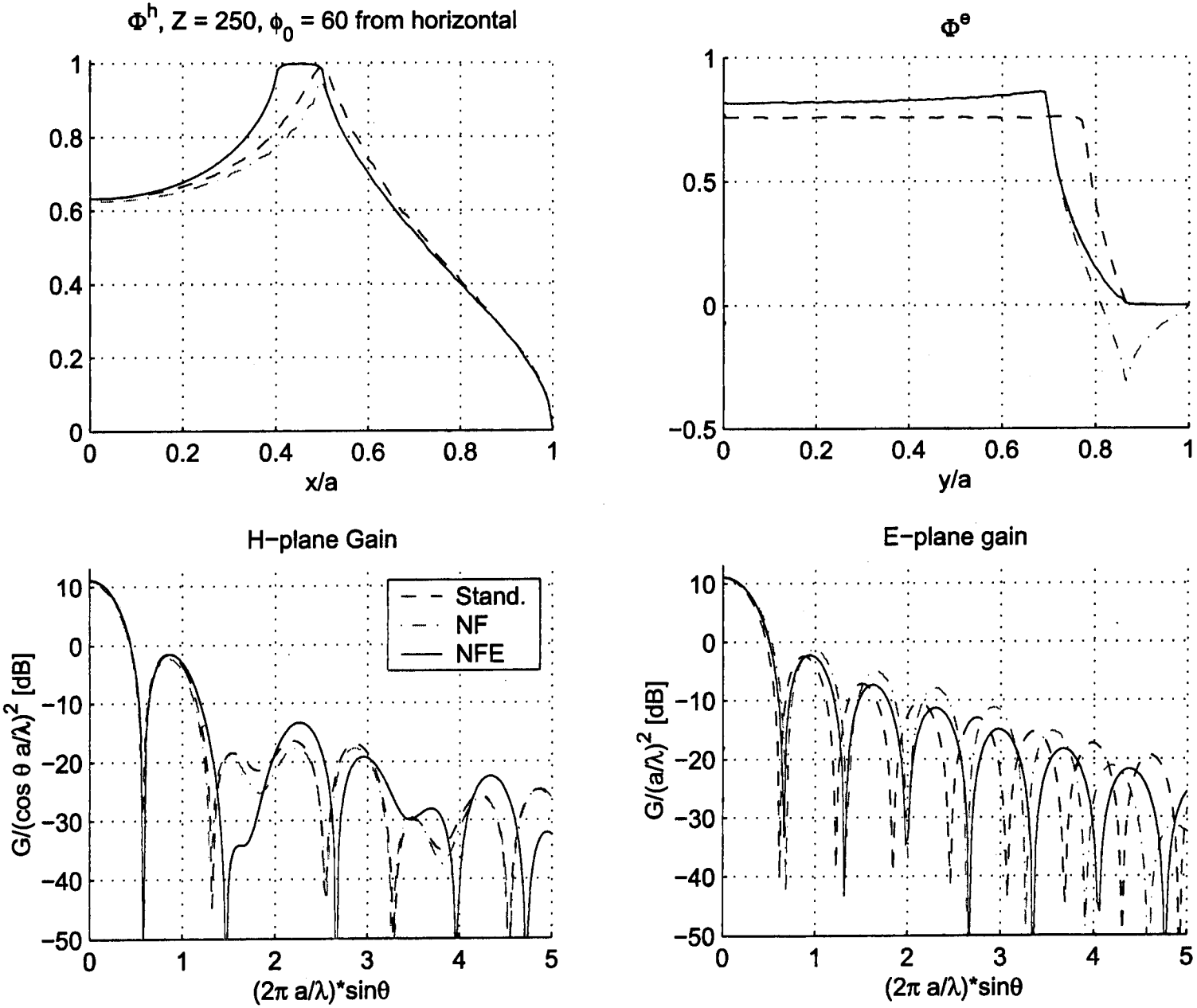

Figure 12: Off boresight radiation in the time- and frequency-domains for Z = 250 Ω, ϕ_0 = 60° in the *E* and *H*-planes.

3.2. Gain Plots

In Figs. 13 and 14 we present the effective gain and effective gain normalized to frequency squared as a function of frequency and angle off boresight in both the *E*- and *H*-planes for the 150 Ω feeds. The normalized gain plots show G/ω^2 for each antenna configuration. Figs. 15 and 16 present the effective gain and normalized effective gain as a function of frequency and angle off boresight in both the E- and H-planes for the 200 Ω feeds. Figs. 17 and 18 present the effective gain and normalized effective gain as a function of frequency and angle off boresight in both the *E*- and *H*-planes for the 250 Ω feeds. All of the gain calculations were completed for an aperture of radius 1 m. Increasing the radius will increase the gain as $(r/a)^2$ and change the angular location of the lobes as described in figs. 7 – 12. The effective gain increases as f^2 as expected for an aperture antenna.

4. Discussion

It is simplest to begin our discussion by noting the variations from the most common case of a 200-ohm feed impedance with a 60-degree arm angle, in the standard feed arm configuration. Switching to the non-floppy feed arms reduces h_a/a by 7%. If the aperture is shaped to avoid the exclusion region, then the reduction is 0.4%, which is negligible. Analogous numbers may be obtained for other cases from Table I.

For the 200 Ω case there are some important items to note.

1. The feed arms at 60° from the horizontal provide 1-2 dB more gain for the three configurations tested.
2. For 45° feed arms, the NFE aperture provides the highest boresight gain. For the 60° feed arms, the NFE and standard aperture provide the same boresight gain, because at 60°, the radius b_2 is farther from the optimum radius than the circle of symmetry. In both cases, the NFE provides 0.7-0.8 dB of additional gain over the NF case.
3. In the *H*-plane, the 60° feed arms provide 4-5 dB more sidelobe isolation than the 45° feed arms. At 60° the NFE provides 0.6 dB over the standard configurations and 0.3 dB over the NF configuration. At 45° the NFE has the *worst* sidelobes.
4. In the *E*-plane, the NFE configuration provides 3.2 dB of additional sidelobe isolation beyond the NF configuration (which is the worst). There is an additional 1 dB of sidelobe isolation at 60° than at 45°.
5. The shape of the beam at 45° is fan in all cases. For the standard configurations, the beam is 50% wider in the *E*-plane than the *H*-plane. For the NF, it is 100% wider, and for the NFE, it is 75% wider. At 60°, the beam is much closer to symmetric. For the standard configurations, the beam in the *E*-plane is 14% wider than in the *H*-plane. For the NF case, it is 50% wider, and for the NFE case, it is 30% wider.

5. Conclusions

We have calculated a number of parameters associated with the high-frequency performance of certain variations of Impulse Radiating Antennas that are useful with flexible feed arms. We have found that moving the feed arms to the non-floppy position slightly reduces the aperture height, but has no effect if the shaped aperture is used. These calculations will be useful when designing, for example, the Para-IRA and Membrane IRA.

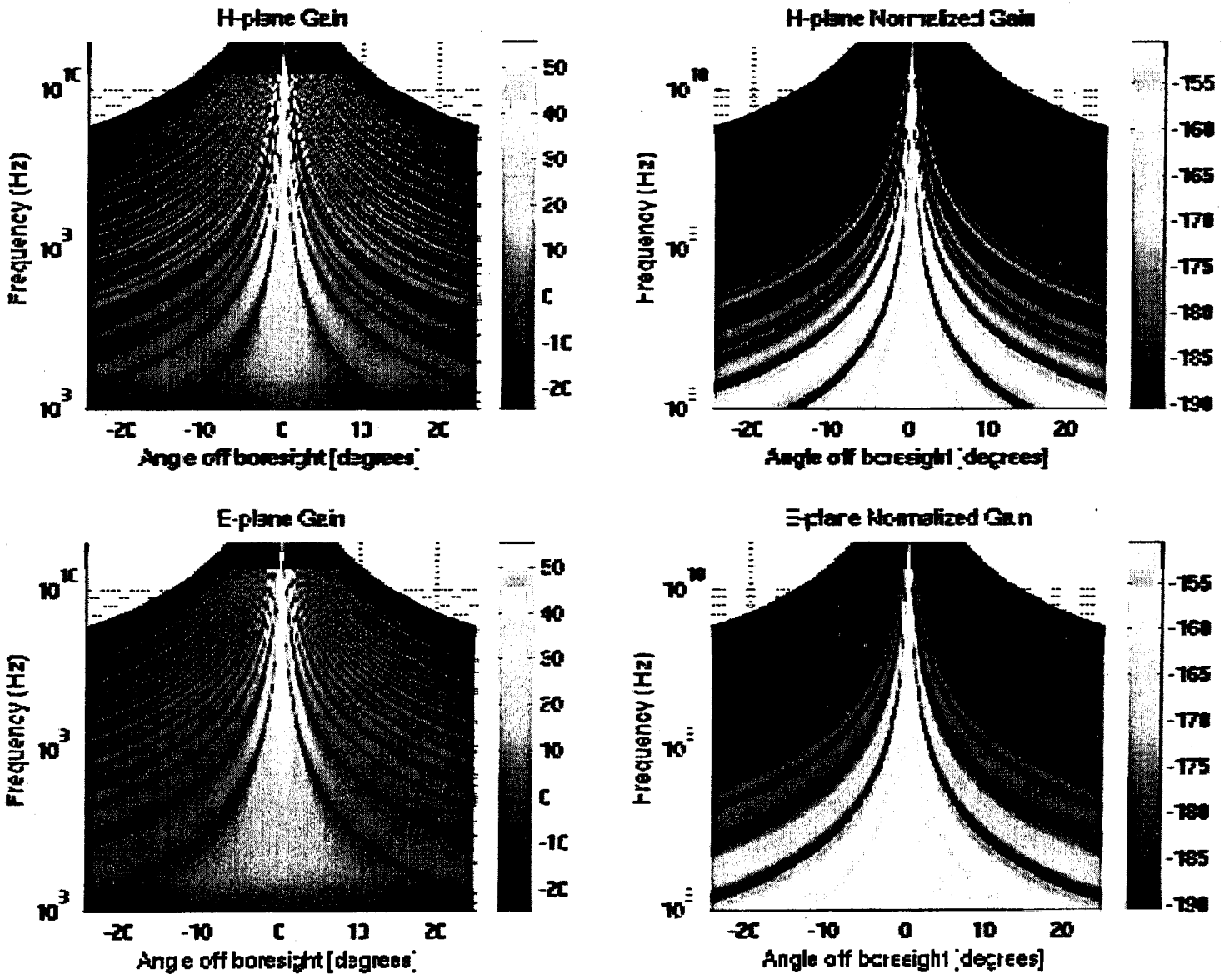

Figure 13: Effective gain for Z = 150 Ω, $\phi_0 = 45°$.

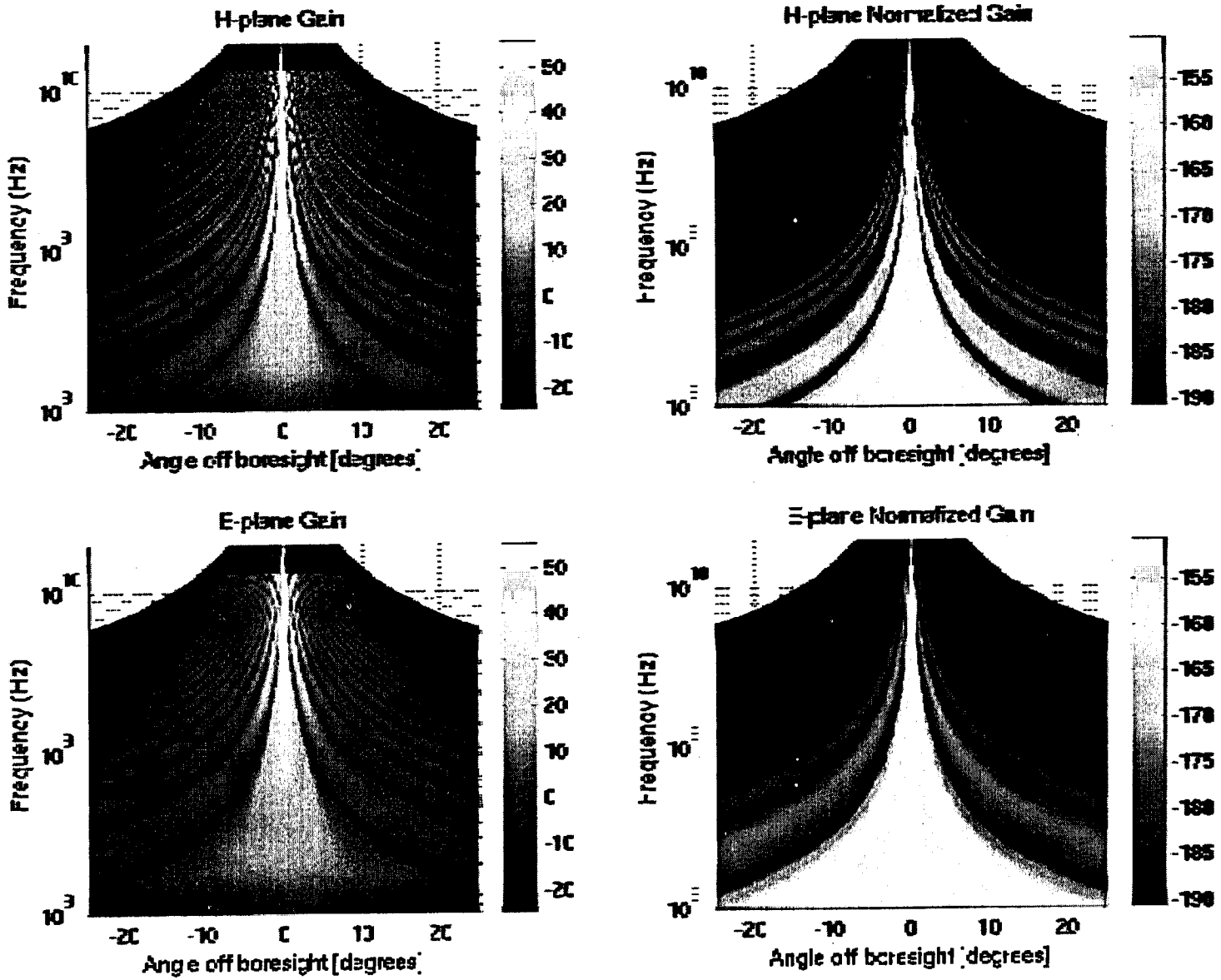

Figure 14: Effective gain for Z = 150 Ω, $\phi_0 = 60°$.

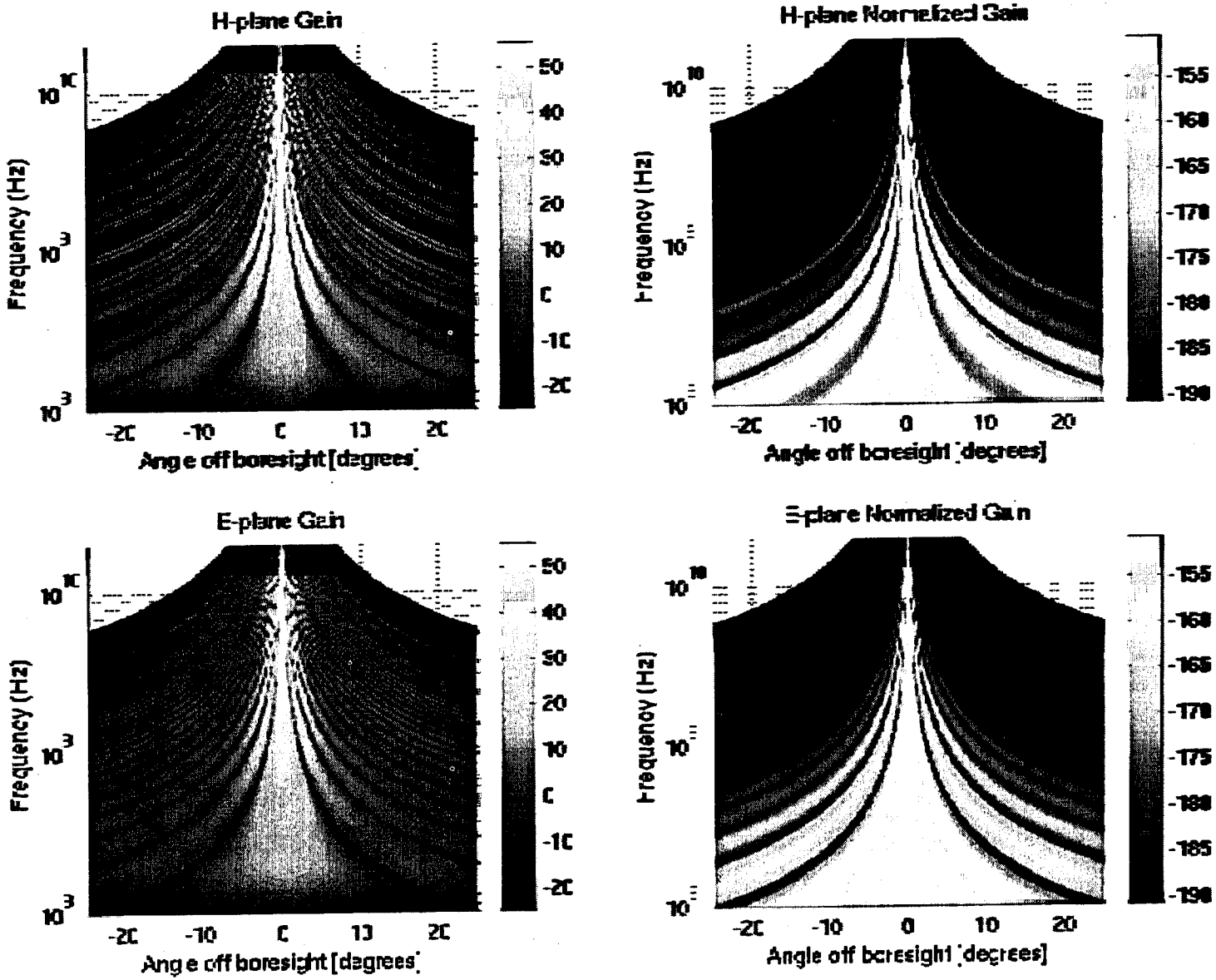

Figure 15: effective gain for Z = 200 Ω, $\phi_0 = 45°$.

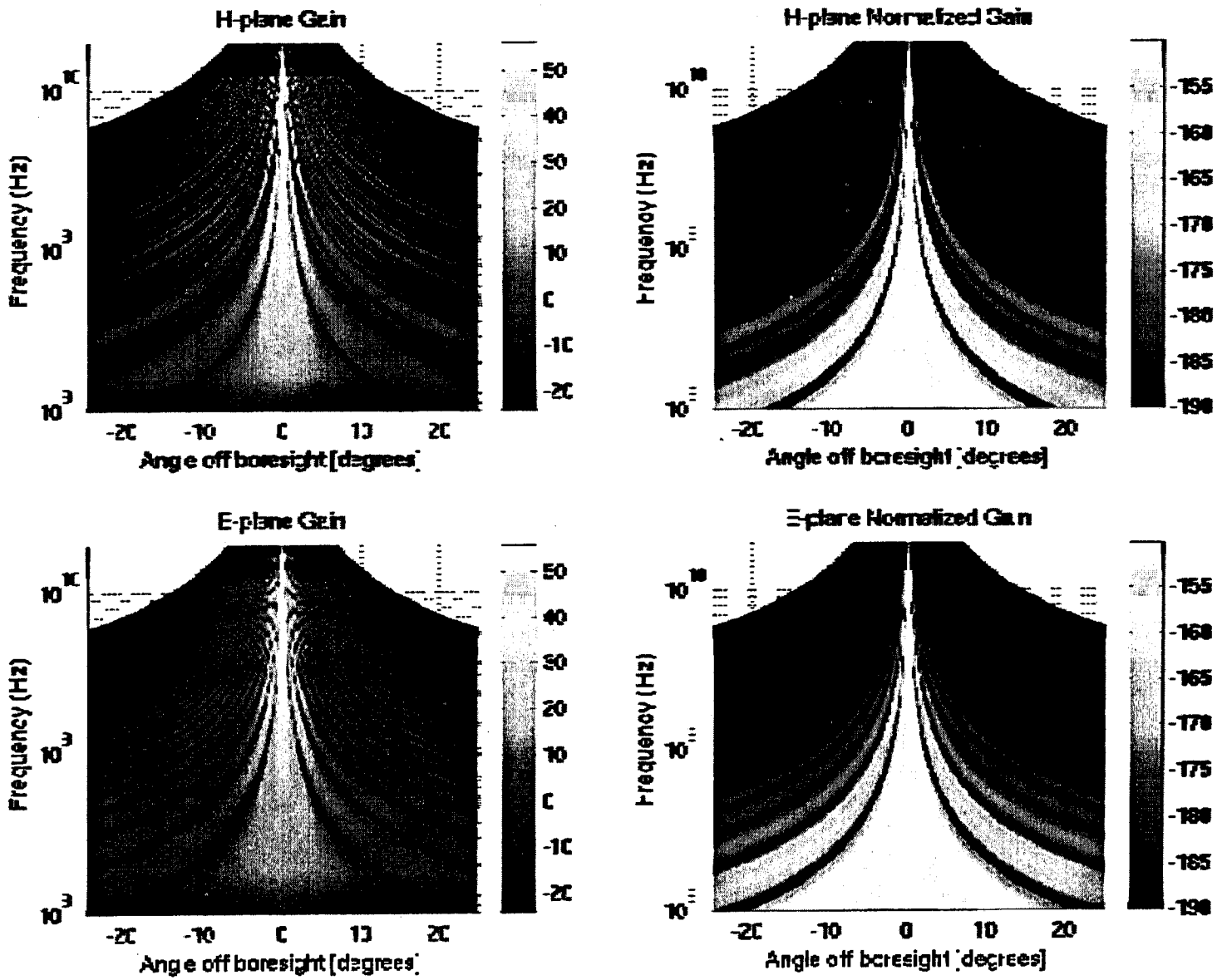

Figure 16 Effective gain for Z = 200 Ω, $\phi_0 = 60°$.

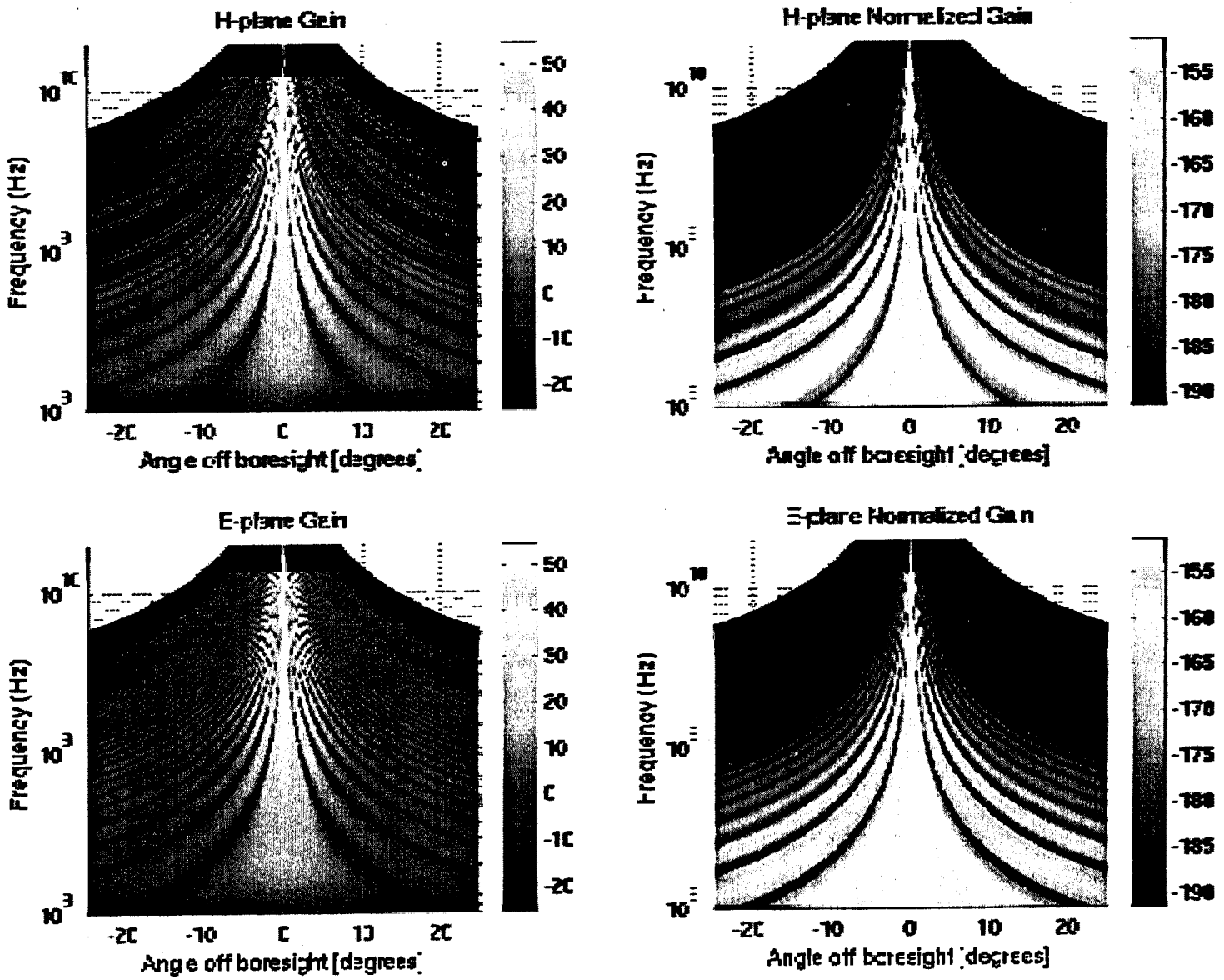

Figure 17 Effective gain for Z = 250 Ω, $\phi_0 = 45°$.

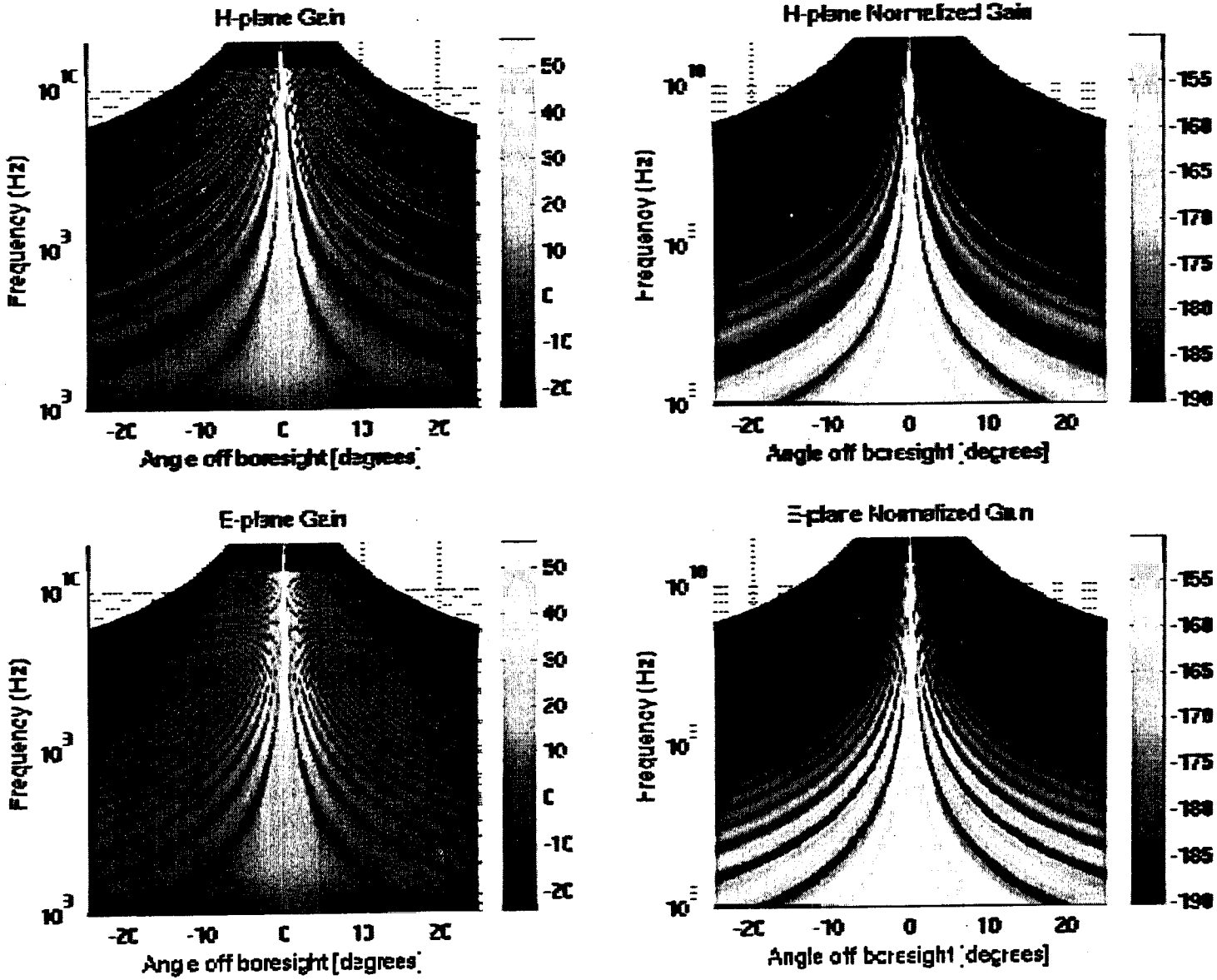

Figure 18 Effective gain for Z = 250 Ω, $\phi_0 = 60°$.

Acknowledgement

We wish to thank the U. S. Army Space and Missile Command for funding this work.

References

[1] L. M. Atchley, E. G. Farr, J. S. Tyo, N. de la Merced, and L. L. Altgilbers, Development and Testing of a Parachute Deployable Impulse Radiating Antenna, Sensor and Simulation Note 465, March 2002

[2] L. H. Bowen, E. G. Farr, J. P. Paxton, A. J. Witzig, C. E. Baum, D. I. Lawry, and W. D. Prather, Fabrication and Testing of a Membrane IRA, Sensor and Simulation Note 464, January 2002

[3] M. J. Baretela and J. S. Tyo, "Selective trimming of impulse radiating apertures to increase prompt radiated fields," Sensor and Simulation Notes #461, C. E. Baum, Ed., (AF Research Lab, Kirtland AFB, NM, 2001) [4]C. E. Baum, E. G. Farr, and D. V. Giri, "Review of Impulse-Radiating Antennas," *Review of Radio Science*, W. R. Stone, Ed., pp. 403 – 439 (Oxford U. Press, New York, 1999)

[5] C. E. Baum, "Aperture efficiencies of IRAs," *Sensor and Simulation Notes* #328 C. E. Baum, Ed., (AF Phillips Lab, Kirtland AFB, NM, 1991)

[6] C. J. Buchenauer, J. S. Tyo, and J. S. H. Schoenberg, "Prompt aperture efficiencies of impulse radiating antennas with arrays as an application," *IEEE Trans. Antennas Propagat.* **49**: 1155 – 1165 (2001)

[7] J. S. Tyo and C. J. Buchenauer, "Experimental verification of the effect of aperture trimming on prompt {IRA} response," *IEEE Trans. Antennas Propagat.* **50**: 1032 – 1034 (2002)

[8] J. S. Tyo, "Optimization of the {TEM} feed structure for four-arm reflector impulse radiating antennas," *IEEE Trans. Antennas Propagat.* **49**:607 – 614 (2001)

[9] L. H. Bowen, E. G. Farr, C. E. Baum, T. C. Tran and W. D. Prather, "Experimental results of optimizing the location of feed arms in a collapsible IRA and a solid IRA," *Sensor and Simulation Notes* #450, C. E. Baum, Ed., (AF Research Lab, Kirtland AFB, NM, 2000)

[10] E. G. Farr and C. E. Baum, "Prepulse associated with the {TEM} feed of an impulse radiating antenna," *Sensor and Simulation Notes* #337, C. E. Baum, Ed., (Air Force Phillips Lab, Kirtland AFB, NM, 1992)

[11] C. E. Baum, "Focused aperture antennas," *Sensor and Simulation Notes* #306, C. E. Baum, Ed., (Air Force Weapons Lab, Kirtland AFB, NM, 1987)

[12] E. G. Farr and C. E. Baum, "Radiation pattern of reflector impulse radiating antennas: early time response," *Sensor and Simulation Notes* #358, C. E. Baum, Ed., (Air Force Phillips Lab, Kirtland AFB, NM, 1993)

[13] C. A. Balanis, *Advanced Engineering Electromagnetics*, (Wiley, New York, 1989).